**RESEARCH ARTICLE**

**Key Points:**
- A seismically active area is recorded using distributed acoustic sensing of a downhole fiber
- We estimate P- and S- wave velocities using fiber data and compare them with conventional surveys
- Velocity analysis unveils a geological structure at the San Andreas Fault Observatory at Depth location

**Correspondence to:**
A. Lellouch,
ariellel@stanford.edu

# Seismic Velocity Estimation Using Passive Downhole Distributed Acoustic Sensing Records: Examples From the San Andreas Fault Observatory at Depth

**A. Lellouch[1]** [ID]**, S. Yuan[1], Z. Spica[1,2]** [ID]**, B. Biondi[1]** [ID]**, and W. L. Ellsworth[1]** [ID]

[1]Department of Geophysics, Stanford University, Stanford, CA, USA, [2]Now at Earthquake Research Institute, The University of Tokyo, Tokyo, Japan

**Abstract** Structural imaging and event location require an accurate estimation of the seismic velocity. However, active seismic surveys used to estimate it are expensive and time-consuming. During the last decade, fiber-optic-based distributed acoustic sensing has emerged as a reliable, enduring, and high-resolution seismic sensing technology. We show how downhole distributed acoustic sensing passive records from the San Andreas Fault Observatory at Depth can be used for seismic velocity estimation. Using data recorded from earthquakes propagating near-vertically, we compute seismic velocities using first-break picking as well as slant stack decomposition. This methodology allows for the estimation of both $P$ and $S$ wave velocity models. We also use records of the ambient seismic field for interferometry and $P$ wave velocity model extraction. Results are compared to a regional model obtained from surface seismic as well as a conventional downhole geophone survey. We find that using recorded earthquakes, we obtain the highest $P$ wave model resolution. In addition, it is the only method that allows for $S$ wave velocity estimation. Computed $P$ and $S$ models unravel three distinct areas at the depth range of 50-750 m, which were not present in the regional model. In addition, we find high $V_P/V_S$ values near the surface and a possible $V_P/V_S$ anomaly about 500 m deep. We confirm its existence by observing a strong $S$-$P$ mode conversion at that depth.

## 1. Introduction

An accurate estimation of the seismic velocity profile is crucial for structural imaging and its ensuing interpretation. It is also important for earthquake location, even though reliable relative locations between clusters of events may be obtained without an accurate model (Waldhauser & Ellsworth, 2000). In conventional seismic processing, retrieving the velocity field above the bedrock is usually a major obstacle (Bakulin & Calvert, 2006). This challenge is due, among others, to a lack of reflection events above the bedrock, velocity variation with depth due to compaction, inhomogeneity in all spatial directions, and the presence of scatterers. Errors in estimating the shallow subsurface velocity deteriorate the image quality of deeper targets (Armstrong et al., 2001; Blias, 2009; Nosjean et al., 2017).

Using downhole measurements can help alleviate some of the difficulties in shallow subsurface velocity estimation (Bakulin et al., 2017). The most widespread method is the vertical seismic profiling (VSP), in which a source is excited at the surface and recorded at different depth levels along the well (Hardage, 2000). Nonetheless, conducting VSP surveys is challenging, as it requires the lowering and clamping of receivers, usually geophones, into a borehole before exciting the source. Such receivers have to withstand harsh temperature and pressure conditions, depending on their depth of installation. In addition, other operations in the borehole are limited during the VSP survey, and such measurements cannot be conducted in a hydrocarbon-producing well. An enticing alternative is the emerging technology of distributed acoustic sensing (DAS). DAS utilizes a fiber-optic cable instead of geophones for seismic sensing along the well (Mateeva et al., 2013). The fiber is probed by a laser interrogator that measures deformation along the fiber due to its interaction with seismic waves. A more detailed description of its operating principles is discussed in *the DAS recording system* section. Fibers can be installed in several different ways that do not interfere with the well (Daley et al., 2013). As the fiber is a passive component, no electronic equipment needs to be lowered down into the borehole, and fibers may be left in the ground for a virtually unlimited amount of time.

In this study, we show how downhole passive DAS records can be used for velocity model estimation. We use earthquakes propagating near vertically and recorded by a DAS downhole array to build $P$ and $S$ velocity models at the borehole location. Relatively weak recorded earthquakes have a wide frequency content, which allows for high-resolution model estimation. In contrary to conventional VSP surveys, this approach does not require a dedicated survey, can be used to directly extract $S$-velocity profiles, is within the far-field limit, and can be repeated at different times at almost no additional cost. Moreover, we show an ambient seismic field interferometry approach, yielding a $P$ wave velocity model. To our knowledge, this is the first application of interferometry to downhole DAS records. It can be especially helpful in seismically quiet areas. We illustrate the application of both methods using the San Andreas Fault Observatory at Depth (SAFOD) main hole, in which a fiber is installed. We compare our suggested approach to a conventional VSP experiment conducted with downhole geophones and a regional model of the area obtained from surface seismic surveys.

## 2. Experimental Setup

### 2.1. The DAS Recording System

During recent years, DAS has been proven apt at recording seismic data at a high spatial and temporal resolution. It has been used for both active surveys and passive monitoring, onshore and offshore, and as a downhole as well as a horizontally installed sensor (Ajo-Franklin et al., 2017; Biondi et al., 2017; Daley et al., 2013, 2016; Dou et al., 2017; Hornman, 2017; Jousset et al., 2018; Karrenbach et al., 2017; Lindsey et al., 2017; Martin, Biondi, et al., 2017; Martin, Castillo, et al., 2017; Martin & Biondi, 2018; Mateeva et al., 2013, 2014. Wang et al., 2018). DAS systems are commonly based on Rayleigh backscattering of a laser pulse propagating through an optical fiber. Due to imperfections in the fiber, some of the propagating energy is reflected back during propagation. When the fiber is stationary, such backscattering is constant. On the contrary, when the fiber is distorted due to an interaction with a seismic wave, some photons are reflected in a different way. An interrogator unit, connected to one end of the fiber, continuously sends short laser pulses through it. Recorded reflected photons undergo interferometry with the reference transmitted pulse, and the resulting phase shift is quasi-linearly proportional to the total strain along the direction of the fiber (Grattan & Meggitt, 2000).

In its simplest form, DAS acts as a strain meter. However, as there is no single DAS architecture, systems operating in time or frequency domain may measure either strain or strain rate, accordingly. The acquisition setup used for this study measures strain with respect to a certain baseline reference, which is the natural backscattering of the fiber. As the speed of light in the fiber is known, the time of arrival of the backscattered energy can be mapped to the distance along the fiber (Parker et al., 2014). By repeating the phase-shift measurement during the pulse propagation time, one can actually compute strain variations in different sections of the fiber. By differentiating these cumulative strain measurements, acquired at different times during pulse propagation, a spatially dependent strain profile may then be obtained. This is the distributed nature of the measurement. If subsequent pulses are generated quickly enough, a strain profile along the fiber can be determined at acoustic frequencies. DAS systems are single component and measure strain or strain rate along the direction of the fiber. Therefore, directivity effects, depending on source radiation pattern, mode of propagating wavefronts, and fiber orientation, are visible in recorded signals (Martin, 2018). In our analysis, we convert strain records to strain rate by taking their derivative in time. This removes the dependency on the natural backscattering of the fiber.

There are many more technical details about DAS systems and their comparison to standard instruments (e.g., Papp et al., 2017). For our purposes, we describe only the gauge length, which is the length over which the phase shifts are measured. It effectively acts as a moving window spatially averaging strain. A detailed explanation of gauge length effects is given by Dean et al. (2017). In short, longer gauge lengths promote higher signal-to-noise ratio while filtering out high-frequency components of the data. In this study, a standard 10-m gauge length was used for data acquisition. It is adequate for typical 0- to 100-Hz recorded events, such as the ones we examine.

### 2.2. The SAFOD DAS Array

A detailed description of the SAFOD experiment can be found in Zoback et al. (2011). In June 2017, an OptaSense DAS interrogator, model ODH3.1, was attached to the longer fiber in the SAFOD main hole,
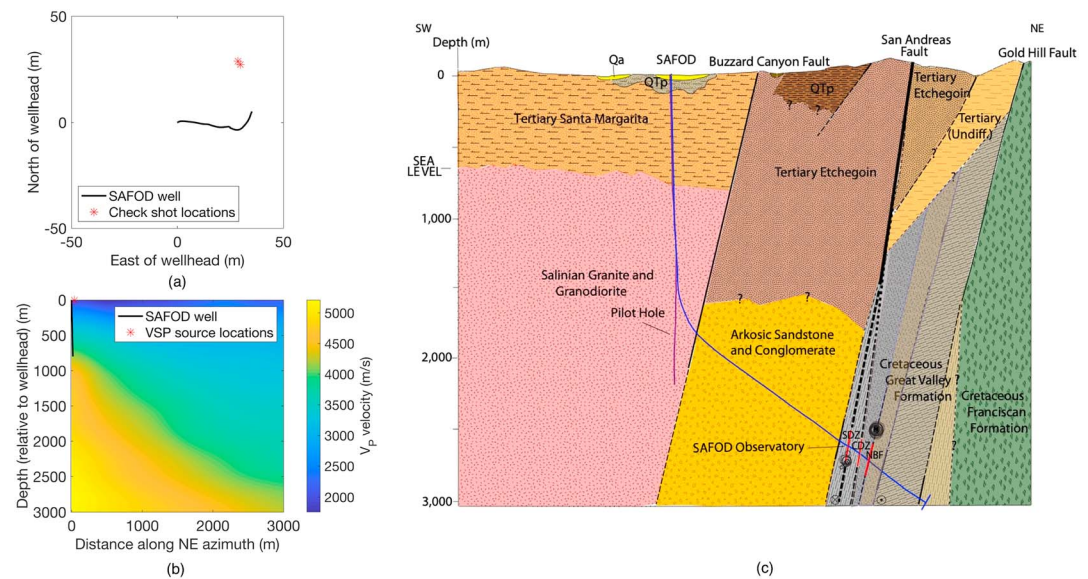
**Figure 1.** The SAFOD borehole in map (a) and side (b) view. The side view is along the NE azimuth, which is perpendicular to the San Andreas Fault. The well trajectory is plotted as a black line. Source locations for the geophone survey are plotted as red stars. A 2-D section crossing the fault zone and taken along the NE azimuth from a regional *P* wave velocity model (Hole et al., 2006) is displayed in the background. In (c), we show a geological overview of the SAFOD experiment (taken from Zoback et al., 2011). The DAS fiber is mostly installed within a sediment area, the Tertiary Santa Margarita. The shallow (< 75m) part crosses alluvial sediments. SAFOD = San Andreas Fault Observatory at Depth; DAS = distributed acoustic sensing; VSP vertical seismic profiling.

reaching a depth of 864 m. The fiber terminates above the basement (granite) contact. Due to a failure of the loop at the end of the fiber, we limit our analysis to a depth of 800 m. The reason for that choice is that starting approximately at the failure depth, the records contain no signal at all. However, in the depth range of ~800 m to the failure depth, the records seem to contain many more noisy channels. While some of the channels appear to be reliable, we suspect that they might be corrupted in some way and thus choose not to use them. The fiber is under a tension of approximately 1 N and housed in a 0.9-mm steel tube cemented between casing strings. We illustrate the area of the well that is covered by our analysis in Figure 1. In the depth range of interest, the well is deviating east. For comparison, we later show the analysis of a geophone survey conducted during 2005 in the same well. Geophones were located roughly every 15 m, starting at a depth of 45 m, and the two explosive sources were more than 40 m away from the wellhead. The goal of that survey was to assess the SAFOD main hole. Since the DAS fiber was deployed and interrogated in the same well, we can compare the two results.

The DAS interrogator can map strain as a function of distance along the fiber. However, distance along the fiber is not necessarily equal to the distance along the well. Mapping fiber distance to spatial coordinates is not trivial (Mateeva et al., 2014) and might require advanced calibration procedures if a simple "stretch" mapping using two reference points cannot be computed. For the SAFOD array, the fiber, a single mode type (model SMF28; see Blum et al., 2008, for details), was put in a steel tube and under tension, and therefore, its length is expected to match the location along the well. However, minor discrepancies may arise due to fiber slack, rotation, and by-design excess fiber length (Madsen et al., 2016). As the initial installation of the fiber was conducted over a decade ago, it is also possible that the fiber underwent environment-induced changes affecting its installation or internal properties. As a side note, it is worth mentioning that the same fiber can also be used as a permanent strain meter, measuring fault-induced displacements. Since a long baseline strain recording of SAFOD was acquired, structural changes could be detected. However, this is not the focus of this study. The recording system was operative for about a month during June-July 2017. Due to technical issues, about 22 days of recorded data are useful. Data were recorded at a 2,500-Hz frequency with a 10-m gauge length and a 1-m channel spacing. The interrogator used in this study measures strain along the fiber.
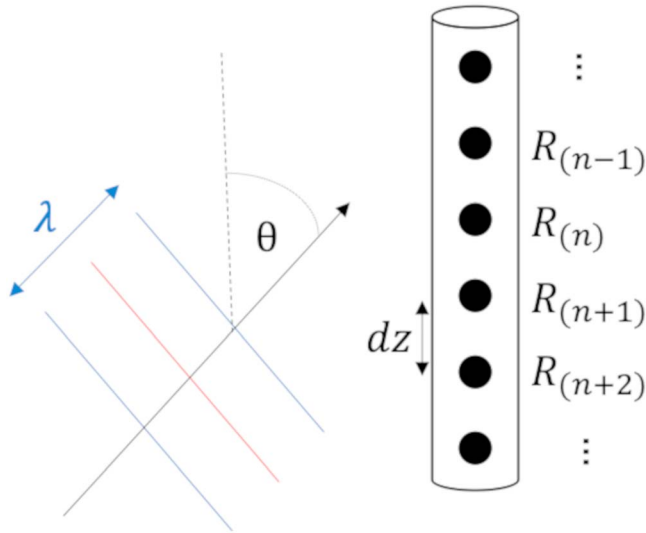
**Figure 2.** Schematic representation of a planar wave-front reaching a discrete downhole array. The distance between receivers, denoted as black circles, is $dz$. The angle $\theta$ marks the angle between the direction of propagation (Poynting vector) and the array, represented by discrete receivers $R_i$. The wavelength $\lambda$ is schematically indicated.

## 3. Velocity Model Estimation Using Earthquakes Recorded by Downhole DAS

### 3.1. Theory

In this section, we schematically describe a uniaxial downhole recording of an incident plane wave (Figure 2). The vertical direction represents depth. We approximate the propagating wavefield as a plane wave recorded by receivers, idealized as a set of discrete points $R_i$ at equal distances, with $n$ being the point's index along the fiber. Assuming the distance between two adjacent measurement points is $dz$, and the angle $\theta$ defined in Figure 2, the arrival time difference between them is, geometrically,

$$t_n - t_{n+1} = \frac{dz \cdot \cos(\theta)}{V}, \tag{1}$$

with $V$ being the wave propagation velocity in the medium, assumed to be constant. $t_n$ is the time of arrival at receiver $n$. This relation can also be generalized for depth-dependent velocity $V$ and varying incidence angle $\theta$. It becomes a locally correct approximation within a region in which the propagating wave can be regarded as a planar one. Nonetheless, the angle of incidence is unknown to us in the general case, and it is impossible to separate subsurface velocity from the incidence angle even if arrival travel times are correctly estimated.

However, using events located directly above or below the DAS array, propagation is guaranteed to be along the direction of the vertical axis, assuming no lateral velocity variation. In this case, the angle of incidence is always $=0°$ or $180°$, and we can compute the average velocity $V_n$ in the interval between the two receivers $[R_n, R_{n+1}]$ by

$$V_i = \frac{dz}{|t_n - t_{n+1}|}. \tag{2}$$

This relation holds at every location along the fiber and may thus be used for continuous estimation of the velocity profile $V(z)$ along it.

In DAS records, strain (or strain rate) is measured along the fiber, which in this study is approximated as vertical. Transforming a point strain measurement to an equivalent conventional geophone, measuring ground velocity along the vertical direction, is based on the following relation:

$$\frac{\partial u_z}{\partial z} = \frac{\partial u_z}{\partial t} \cdot \frac{\partial t}{\partial z} = \frac{\partial u_z}{\partial t} \cdot \frac{1}{v}, \tag{3}$$

where $u_z$ is the particle displacement in the $z$ direction and $1/v$ is the local apparent slowness. This slowness depends on both subsurface velocity model $v$ and the wavefront's angle of incidence. While the $1/v$ scaling may influence the amplitude of recorded data, it does not change its phase. Therefore, any travel time-based analysis, using earthquakes or the ambient seismic field, should yield the same result for both DAS and geophone-equivalent data. In addition, DAS is not a point measurement, and gauge length effects may affect phase by distorting wavelets (Dean et al., 2017). However, as previously stated, the gauge length is adequate for recorded events of interest, and we do not observe any noticeable wavelet distortion. We compute strain rate by applying a time derivative to recorded strain data. Since the subsurface velocity $v$ (equation (3)) is constant with respect to time, this amounts to using accelerometer-equivalent data, and the scaling relations remain unchanged.

DAS systems have two major benefits in terms of velocity model estimation. Their spatial density allows for high-resolution analysis, and the fiber installation is permanent. In this study, we suggest using earthquakes recorded by DAS arrays for velocity model estimation. Such earthquakes have to fulfill two major criteria. First, they have to induce strain that is measurable by the vertical DAS array with a high enough signal-

to-noise ratio. This is a function of source moment, focal mechanism, and distance from the array. Second, they have to reach the array in a near-vertical incidence angle. An ideal earthquake for velocity estimation would be located directly below the array. As such, primary phase wave propagation is 1-D, and equation (2) can be directly applied. However, many other earthquakes may still be used. The correction term depending on the angle of incidence $\theta$ is proportional to $1/\cos(\theta)$. A local incidence angle of 10° induces a minute 1.5% increase in the estimated velocity. As the velocity field between the source and the array also influences the direction of propagation, it is not enough to know the source location to compute the angle of incidence. In general, earthquakes originate at far larger depths than the recording array. As velocity is often increasing with depth, the shortest trajectory from source to receiver will bend toward a vertical path, following Snell's law. Therefore, the true incidence angle will be closer to zero (vertical incidence) than its angle computed by a straight line from receiver to source. Consequently, in practice, angles of up to 15-20°, computed along a straight line, are acceptable. Assuming such earthquakes are present, this approach does not require the deployment of a source, can be repeated for different adequate earthquakes, and does not suffer from the near-field limitations often present in VSP surveys due to proximity of the source to the recording array (Landrø, 1999). In addition, since only differential travel times are used, the source origin time is irrelevant and does not need to be known.
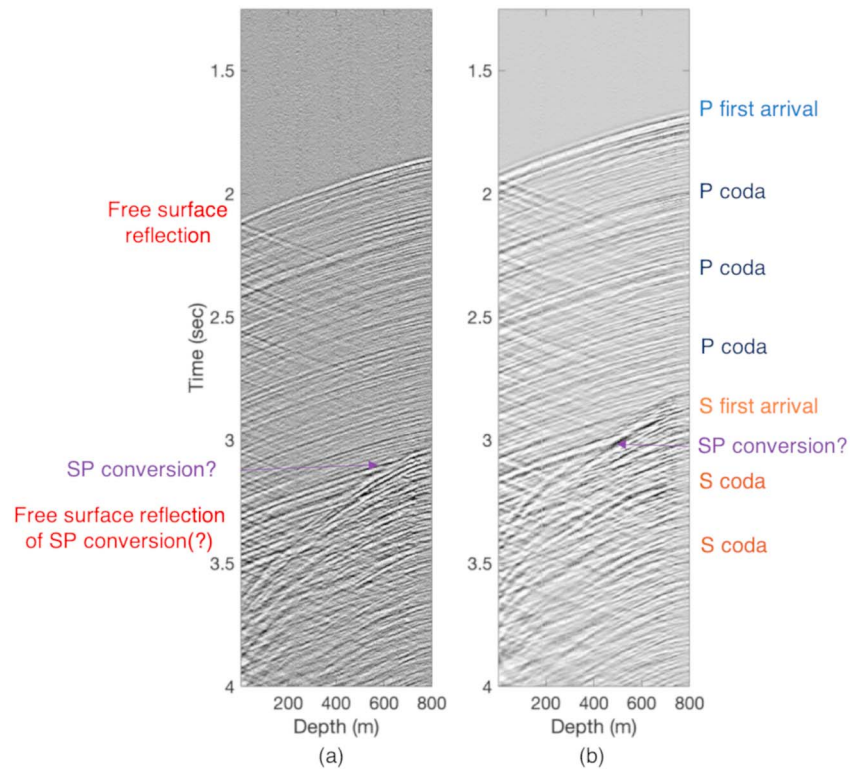
### 3.2. Recorded Earthquakes

For this study, we observe two earthquakes recorded by the array. Both were chosen using the U.S. Geological Survey catalog in that area. Using event timing, relevant DAS data were extracted. The first event is a magnitude $M = 1.33$, located at a depth of $Z = 11.16$ km and at a horizontal distance of $H = 1.87$ km from the wellhead. The second is $M = 2.46$ km located at $Z = 11.43$ km and $H = 2.49$ km. For a uniform half-space, their angles of incidence at the bottom of the array would be about 10.2° and 13.2°, respectively. Since they are located at great depths, at which velocity is higher, we expect significant ray bending. A regional model of the area (Bleibinhaus et al., 2007; Hole et al., 2006) estimates $P$ wave velocity along the array at about 2,500 m/s (close to the surface) to 4,000 m/s (bottom of the array). Velocities of 6,000 m/s are observed at depths of 5-6 km, and it can be expected up to the depth of the earthquakes. Therefore, even using a conservative correction, the angles of incidence at the array would be 6.8° and 8.7°, respectively. This amounts to an average <1% correction of the velocity at the bottom of the array, which is where the incidence angle has the highest impact. Due to velocity increase with depth along the array, the effect would be smaller as we get closer to the surface. Overall, having shown that the error can be safely bounded by an average 1% over-estimation of the velocity, we will treat recorded events as vertically propagating.

In Figure 3, we show recorded earthquakes. Noisy traces are automatically detected and set to zero amplitude. We also apply a trace-by-trace normalization to enhance events. The $M = 1.33$ is in Figure 3a and the $M = 2.46$ in Figure 3b. The same ordering will follow for the rest of the paper. Notable events are marked in the figure. There are noticeable differences in terms of signal-to-noise and frequency range between the two earthquakes. The larger $M = 2.46$ earthquake in Figure 3b has lower frequency content, visible especially in the first arrival $P$ waves. It also has a higher signal-to-noise ratio, as can be seen by the level of noise preceding the first arrivals. Due to technical issues with file headers for the earthquake in Figure 3b, absolute time is only approximated. However, the two events seem to have similar behavior and arrival moveouts. For all subsequent velocity estimation purposes, only the $M = 1.33$ event is used. The reason is that for the $M = 2.46$ event, we could not coherently follow the first $S$ wave arrivals. Since we aim for a fair comparison between different methods, we choose to base our analysis on a single event for all of them. In addition, the average maximal usable frequency of the $M = 1.33$ event is around 70 Hz. The $M = 2.46$ has, as expected, a lower frequency content; thus, we prefer to use the weaker earthquake for the benefit of increased temporal resolution at the price of lower signal to noise.

### 3.3. Estimating Velocity by Travel Time Picking

We begin by estimating the $P$ wave velocity along the array. The first arrival phase is picked for both earthquakes. It is conducted using a linear programming approach, aiming at maximizing total energy along a picking path. However, many other choices of picking approaches are possible. We follow Molyneux and Schmitt (1999) but use the total signal amplitude as the objective function in order to be able to follow a specific polarity. Specifically, we follow the negative amplitudes (black in Figure 3). After the picks have been established, we detect the nearest earlier zero crossing (change from positive to negative value) and adjust

**Figure 3.** Earthquakes recorded in San Andreas Fault Observatory at Depth distributed acoustic sensing array, filtered in the 0- to 120-Hz range. $M = 1.33$ (a) and $M = 2.46$ (b) events are plotted. Many different phases are present, some of which are indicated by text alongside the seismograms. Unless an arrow is present, the text matches the time of arrival of the event. In addition to direct $P$ and $S$ arrivals, we clearly observe $P$ and $S$ coda events, possible $SP$ conversions, and free surface reflections of all phases.

the picks to that sample, as we found it more stable. Picks at noisy trace locations are linearly interpolated with their nearest neighbors, and all picks are subsequently smoothed using a 50-m moving average window. In Figure 4, we show the first break picking results for the $P$ wave arrivals. They are shown in blue in Figures 4a and 4b, overlaying recorded data. Then, data are shifted according to picked times. We will refer to this type of correction as a moveout correction because after it is applied, recorded events should have no moveout. It can be applied in either time or temporal frequency domain. If the time domain is chosen, proper interpolation is required. However, it is better to apply it in the frequency domain. We then use zero-padded traces to avoid cyclic wraparounds. Here, we apply this moveout correction for $P$ waves. In Figure 4c, the moveout-corrected first arrivals appear as flat, and picking seems to be reliable. For Figure 4d, the last 20 m is misaligned with the rest of the record. However, we do not analyze velocities in those areas, as they are too close to the fiber's edges and cannot be properly smoothed. It is also interesting to observe that after moveout correction, $P$ coda events in both Figures 4c and 4d seem well aligned. However, they maintain a slight misalignment when compared to the first arrivals. This indicates that they have propagation velocities similar to first $P$ wave arrivals but reach the array in a slightly different angle of incidence. This may be explained by small differences in propagation path from source to receiver array, but this statement cannot be validated. As previously mentioned, only the picks in Figure 4a are used for velocity analysis.

Picking of $S$ waves is more challenging than $P$ waves due to several factors. First, for far vertically or near vertically propagating earthquakes, the fiber sensitivity to $S$ waves is greatly diminished. As DAS measures strain along the fiber, an $S$ wave propagating parallel to the array should not, in theory, be recorded, as all particle motion is in perpendicular directions. Due to the complex well structure, including the casing, cement, steel tube, and fiber coupling, $S$ waves are still visible, albeit possibly in lower quality. Second, the direct $S$ waves that we aim to pick undergo severe interference with other phases in play: $P$ coda, $SP$ mode conversions, free surface reflections of earlier phases, and so forth. Finally, the fact that there is no
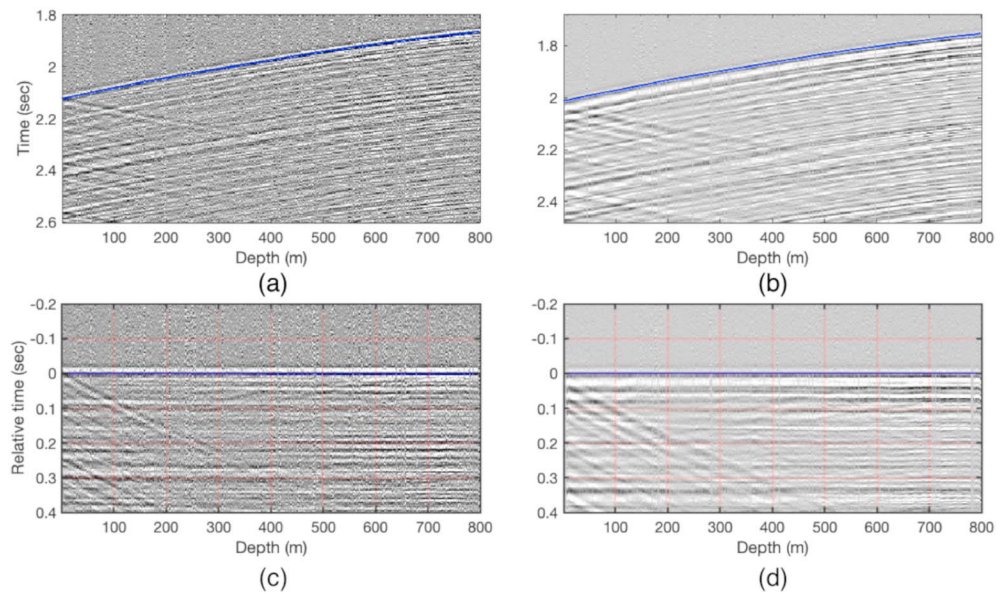
**Figure 4.** *P* wave arrivals and their picking for both earthquakes, shown at 0–120 Hz. (a) and (b) are zoomed-in versions of Figure 3. First-break picking is overlaid in blue, indicating the zero crossing between positive (white) and negative (black) phases. In (c) and (d) we show the same records after a moveout correction based on picked times. The zero relative time is shown in blue. For the event at (d), the 780- to 800-m range seems problematic. However, this area is not used for analysis, as it is too close to the edge of the array.

clear "silence" period preceding them can pose a difficulty for many picking algorithms. In order to cope with these challenges, preprocessing is applied to *S* waves records. The different stages are summarized in Figure 5. The *S* phase of the $M = 1.33$ earthquake is shown in Figure 5a. We apply a moveout correction based on *P* wave picking, the result of which is shown in Figure 5b. This record can now be easily filtered in the $f - k$ domain. We design a filter that allows only for upgoing events with a velocity lower than 11 km/s. After moveout correction, *P* events have an infinite (or near-infinite) velocity and are thus filtered out. Free surface reflections are downgoing and thus filtered out as well. We also limit our processing to a 10- to 80-Hz frequency range. Data after applying $f - k$ filtering are shown in Figure 5c. Despite some residual interferences, the *S* phase is easier to follow. In order to facilitate automatic picking, we apply another moveout correction, this time with an approximated *S* velocity. We assume $V_P/V_S = 1.9$ and compute the expected moveout for *S* waves. Since a *P* moveout was previously applied, we use the residual moveout, computed by *S-P*, for the second moveout correction. After doing so (Figure 5d), the record is significantly flatter, especially in the deeper part of the array. It is then picked automatically, following the negative (black) phase. Picks after a necessary manual editing are overlaid in red. Finally, the same picks are overlaid on the filtered but unshifted data (Figure 5e). Picks seem to consistently follow the same arrival phase. However, there seems to be clear interference with other seismic phases, causing picking errors. Such errors are expected to yield noisy velocity models. Despite these limitations, it would have been more challenging to pick the recorded data directly, probably inducing much larger errors. Estimated velocity models for both *P* and *S* phases are shown in Figure 9.

### 3.4. Estimating Velocity by Local Slant Stacks

Travel time picking suffers from inherent limitations (Lellouch & Reshef, 2019). First, it is conducted channel by channel, which dictates operation in low signal-to-noise ratio. This is especially problematic in DAS records, in which individual channels are often noisier than conventional clamped receivers (Daley et al., 2016). In addition, picking often has to be manually guided and adjusted, which is time-consuming, error-prone, and can be hard to reproduce. Therefore, we suggest an alternative approach, which is based on local slant stack decomposition (Biondi, 1992). It is an array-based processing technique, which aims at measuring data coherency along various possible linear velocities, represented by different slowness values *p*. The computed slowness's range and discretization are chosen according to prior velocity model knowledge
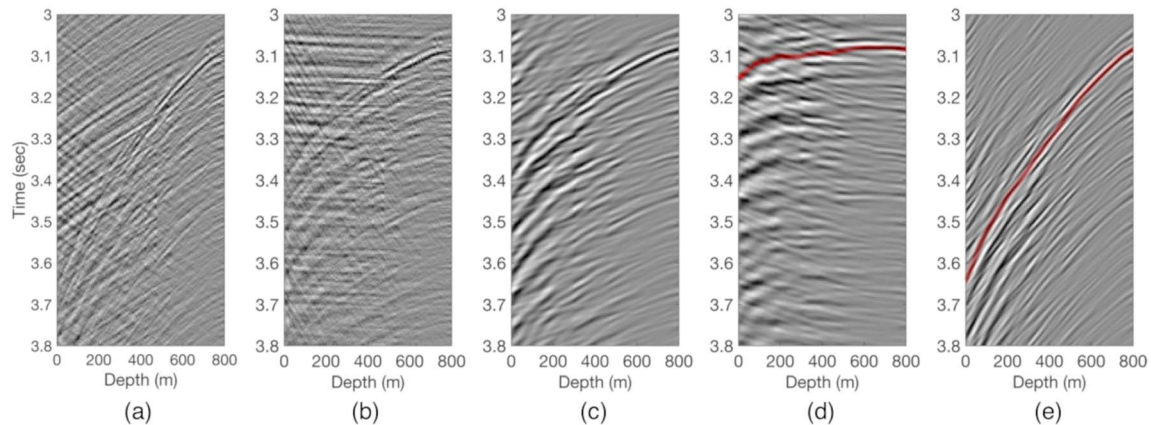
**Figure 5.** *S* wave processing, filtered at 10–80 Hz. (a) Recorded *S* phases for the magnitude *M* = 1.33 earthquake. (b) Record after moveout correction for *P* waves. (c) Moveout-corrected record after $f - k$ filtering. (d) Approximate correction for *S* velocity and results of picking (in red). (e) Same picks overlaid on the filtered, unshifted data. Moveout-based filtering greatly simplifies the picking task.

and resolution needs. In our examples, we scan a velocity range of 300 to 6,000 m/s, computed by 30 m/s intervals. Coherency is computed within a certain channel window, which is chosen according to the recorded arrivals' curvature. In other words, the window has to be small enough so that the recorded arrivals can be approximated by a linear slope. On the other hand, the resolution of the velocity estimation increases with window size. We choose this window as a truncated Gaussian G(z) of 150-m width, with a maximum of 1 at the center channel and a value of $1/e^2$ at the edges of the window. We denote each window by its center channel depth w and one-sided width W. We use a windowed semblance measure (Neidell & Taner, 1971) to estimate data coherency. Semblance is measured in a time window of size [−T,T]. The choice of T is dictated by recorded data frequency. Mathematically, the local slant stack S of recorded data d, ordered as {channel, sample}, is the following mapping:

$$
S(w, p, t) = \frac{\left( \sum_{s=t+p\cdot dz\cdot z-T}^{t+p\cdot dz\cdot z+T} \left[ \sum_{z=w-W}^{w+W} G(z)d(z, s) \right]^2 \right)}{\left( [2W + 1] \sum_{s=t+p\cdot dz\cdot z-T}^{t+p\cdot dz\cdot z+T} \sum_{z=w-W}^{w+W} G(z)^2 d(z, s)^2 \right)},
\tag{4}
$$

in which *p* is the slowness, dz is the distance between adjacent channels, and t is the event origin time. Panels are computed with a single channel overlap. In Figure 6, we show representative slant stack panels computed for three different channel windows. *P* velocity events are easy to detect since they have a clear first arrival (around t = 2 s). Many subsequent events have approximately the same velocity. About 1.25 s later, *S* velocity phases appear. There are several events with a similar *S* velocity occurring at different times. However, *P* events are still simultaneously visible, and interference between the *P* and *S* velocities occurs. This might cause overestimation of the *S* wave velocities. We emphasize that the slant stack method we apply is a basic approach and more advanced methods have been successfully applied to diminish the interference between waves of different velocities (Kostov & Biondi, 1989). Due to the large number of different panels, an automatic method for their analysis is required. We begin by estimating the *P* velocity. For the *P* phase, the first arrival time at the bottom of the array is quite accurately known from the first break picking procedure described earlier. Therefore, for each panel, we look for the maximal coherency value within 200 ms of that estimated arrival time. The chosen velocities are shown in red dashed lines. Thus, we ensure we are not taking into account later events that have a *P* wave velocity. The most stable velocity is estimated from the first breaks, and later events, notably coda, can detract the analysis. For *S* velocity estimation, a longer temporal window is used. Since the arrival time estimated from picking is less reliable, we search for the maximal coherency value within 600 ms of it. In addition, within that window, only velocities of up to 65% of the estimated *P* velocity are allowed. The chosen values, adhering to that condition, are plotted in dashed black lines. Without this step, the maximum semblance could represent a *P* velocity event, as in Figure 6a. This procedure is repeated for every depth window, and estimated velocity models for both *P* and *S* phases are shown in Figure 9.
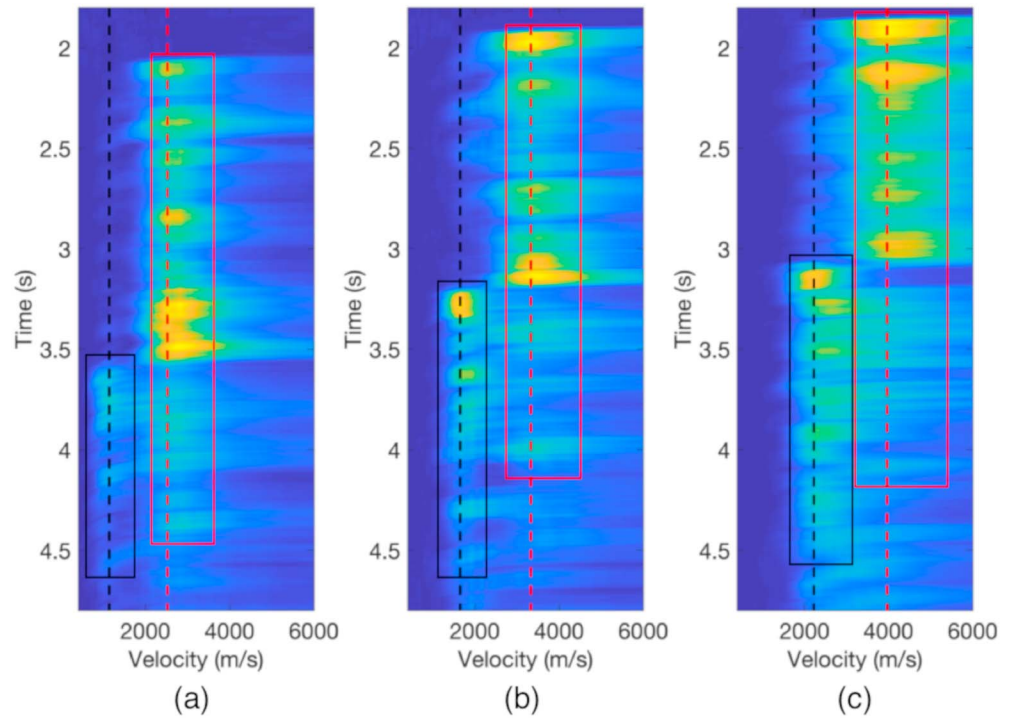
**Figure 6.** Slant stack panels computed for the M = 1.33 event at different depth locations: 0-150 m (a), 275-425 m (b), and 650-800 m (c). *P* wave velocity events are approximately denoted in red boxes while *S* wave velocity events are in black boxes. The automatically estimated velocities are marked by dashed lines of matching colors. For all displayed panels, there is some interference between *P* and *S* events at later (>3 s) arrivals time.

## 4. Other Downhole Velocity Estimation Methods

### 4.1. Ambient Field Interferometry

Retrieving surface wave response between pairs of horizontal DAS sensors using cross-correlation method (Shapiro & Campillo, 2004) has been recently shown by Martin et al. (2018) and Zeng et al. (2017). Here, we show that body *P* wave velocities can also be retrieved using ambient field borehole interferometry between pairs of adjacent overlying sensors (Miyazawa et al., 2008).

The ambient recorded field consists of strain (or strain rate) measurements at different depth locations. As previously discussed, the difference between strain and velocity measurements is scaling by the velocity (equation (3)). Therefore, conventional interferometry methods, which do not take amplitude information into account, can be used directly for DAS data. The cross-correlation $C_{A,B}$ between two strain ($\varepsilon$) measurements at depths $z_r$ and $z_s$ is given, in the frequency domain, by

$$C_{A,B}(\omega) = \langle \varepsilon_{z_s}(\omega) \cdot \varepsilon_{z_R}(\omega) \rangle, \tag{5}$$

where $\langle \, \rangle$ denotes an averaging operator. The imaginary part of the Green's function $\mathscr{G}$ between two sensors, $\text{Im}[\mathscr{G}](z_s, z_r)$, is inferred from the average correlation using

$$\text{Im}[\mathscr{G}] \propto \frac{\langle \varepsilon_{z_s}(\omega) \cdot \varepsilon_{z_R}(\omega) \rangle}{|S(\omega)|^2}, \tag{6}$$

as in Spica et al. (2018) and where $|S(\omega)|^2$ is the power spectrum of the ambient field (Wapenaar & Fokkema, 2006). In Figures 7a and 7b, we show two different possible geometries for borehole interferometry. In Figure 7a, the virtual source $z_s$ is fixed at the top channel, and the virtual receiver $z_r$ varies along the array in 50-m increments. In Figure 7b, the distance between $z_s$ and $z_r$ is constant and set to 50 m. Only the ambient seismic field is used for computing cross-correlations, and the influence of earthquakes is reduced via a running-absolute-mean normalization (Bensen et al., 2007). Correlations are computed using 1 day of
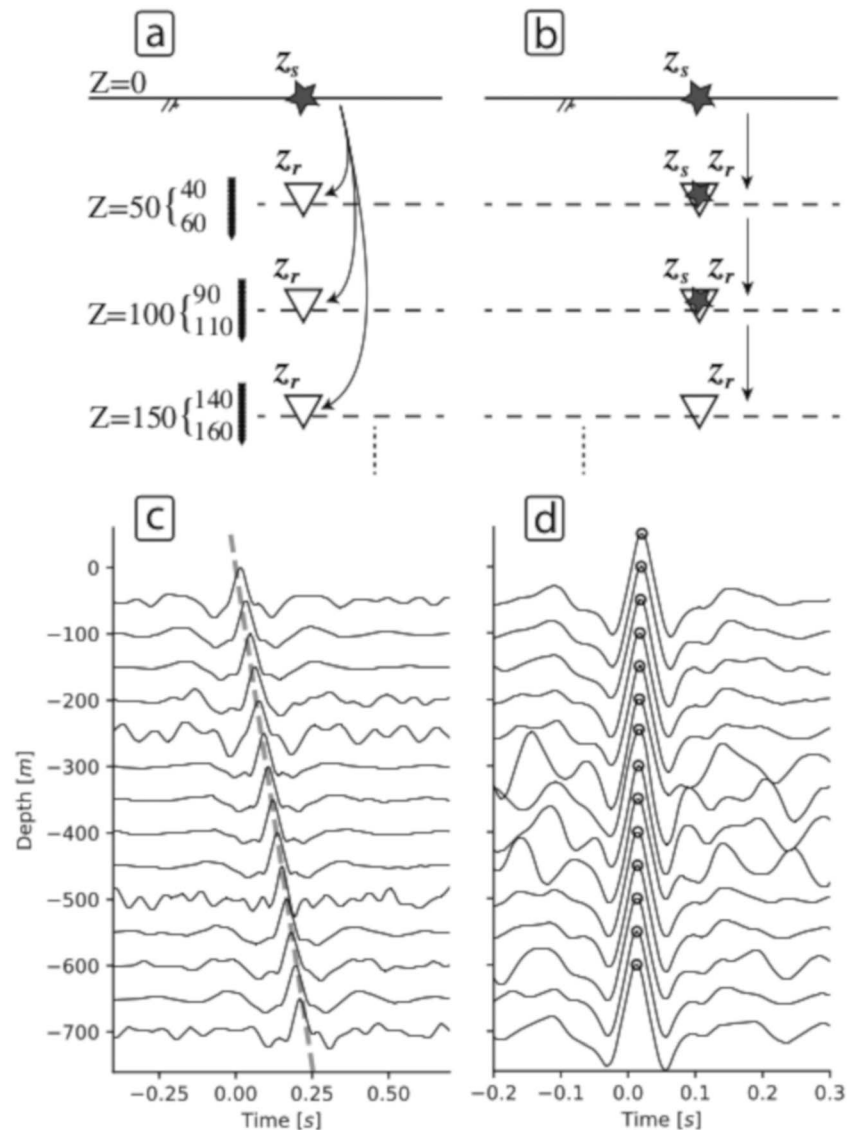
**Figure 7.** Two different geometries used for borehole interferometry. Cross-correlated waveforms are filtered at a 5- to 20-Hz range. In (a), the source is fixed at the top channel, and cross-correlations are computed with different receivers. In (b), cross-correlations are computed between source-receiver pairs of constant distance, and the same spatial locations are used as both virtual sources and receivers. In (c) and (d), we show cross-correlation results obtained with 1 day of data for the geometries showed in (a) and (b), respectively. In (c), the gray line depicts the average 3,200 m/s $P$ wave velocity. In (d), the black circle depicts the picked travel times of the $P$ waves.

continuous data. Records are separated into 30-s windows with a 50% (15 s) overlap. To enhance their signal-to-noise ratio, we compute correlations for nearby source-receiver pairs and stack them. These correlations are calculated using the same source channel but different receiver ones. As previously noted, the source channel $z_s$ may be either fixed at the top of the array or vary along it by 50-m intervals. Stacked correlation values are, in this study, computed by $\overline{C_{S,R}} = \sum_{Z=R-10}^{R+10} C_{S,Z}$. This induces a smoothing of the velocity model but is required to extract a clear signal. Since events within the depth range used for averaging are expected to have different time lags, we apply travel time shifts to the computed cross-correlation functions before stacking them. The shifts are computed using an average 3,200 m/s velocity (Figure 7c). This shift is applied only after an average velocity has been obtained using simple stacking.

Figures 7c and 7d show the resulting stacked correlations in the time domain after a 5- to 20-Hz bandpass filter. An impulsive arrival is observed on the causal side of the correlation functions. The strong signals of these downgoing waves compared to the upgoing ones suggest that the dominant ambient field sources originate at the surface (Zhou & Paulssen, 2017). In Figure 7c, we observe a clear wave packet with an apparent velocity of about 3,200 m/s, which corresponds to an average *P*-wave velocity in the vicinity of the array. Thus, we deduce we are observing a *P* wave and take the correlation functions shown in Figure 7d to estimate its velocity every 50 m.

We estimate the arrival time by seeking the three adjacent samples with the largest correlation values and applying quadratic interpolation to find the time at which the cross-correlation function is maximal (Nakata & Snieder, 2012). It represents the travel time for a *P* wave that propagates between source and average receiver location. In addition, we compute the average *P* wave velocity by performing the same analysis using seven different days of recorded data. The standard deviation at different depth intervals, estimated in 50-m blocks, is between 70 and 90 m/s, depending on the depth of interest. The estimated *P* wave velocity model is shown in Figure 9.

### 4.2. Conventional Geophone Survey

A VSP survey was conducted in April 2005 by the U.S. Geological Survey using a downhole 3-C geophone array contributed by Paulsson Geophysical Services Inc. Explosive sources were detonated more than 40 m away from the wellhead at a depth of about 3 m (Figure 1). Explosive sources in this configuration do not generate visible *S* waves that can be used for velocity analysis. Therefore, we focus on *P* wave model building, conducted with the vertical recording component. Data recorded for the two different explosive sources are shown in Figure 8, with overlaying picked arrivals (red). The average maximal usable frequency is about 55 Hz. It is important to remember that the shallow subsurface induces noticeable dissipation on recorded signals, leading to the relatively stronger loss of high frequencies. Thus, even explosive sources can reach downhole receivers with a relatively narrow frequency content. The picking procedure that was described in the *P wave picking* section is applied here, following the positive (white) phase instead. The choice of phase to pick depends on recorded signal wavelet. Picking here is unambiguous set aside one noisy trace for which the pick was interpolated. However, since sources are excited from an offset, processing must be adapted. For a 1-D experiment, the interval velocity is computed by $\frac{dz}{dt}$, with $dz$ being the depth difference between receivers and $dt$ the difference between picked arrivals. Here, we take the 3-D Euclidean source-receiver distance $D$ and compute interval velocity by $\frac{dD}{dt}$ instead. For near-vertical propagation, this first-order correction is acceptable. A full solution would take into account true propagation paths and their differences, but it requires an initial velocity model. The estimated *P* wave velocity model, computed as an average of the two sources, is shown in Figure 9.

## 5. Models Comparison, Interpretation, and Uncertainty

In this section, we summarize all the extracted velocity profiles. Picks, their difference, and the estimated velocity all require smoothing. We follow the same smoothing parameters for all data sets, and the largest operator is 100 m long. Slant stack results are also smoothed with the same 100-m window. Results are summarized in Figure 9. There are seven different velocity models, five of which are for *P* wave velocity. The first two models we display are estimated using the $M = 1.33$ earthquake. They are computed using slant stacks (solid blue) and travel time picking (solid red), accordingly (sections 3.3 and 3.4). We display the *P* model (dashed black) computed from the conventional geophone survey (section 4.2) and the model extracted using ambient field interferometry (solid green, section 4.1). In dotted cyan, we plot a regional *P* model, obtained from surface seismic surveys (Bleibinhaus et al., 2007; Hole et al., 2006). We could obtain *S*-wave velocities only when using the $M = 1.33$ earthquake and thus display the velocities estimated using slant stack (dotted blue) and picking (dotted red), respectively. We also display the computed $V_P/V_S$ for both slant stack and travel time picking analysis.

Velocity models obtained using slant slack and travel time picking of the recorded earthquake are very similar to the results of a conventional downhole survey processing. Quantitatively, the average difference between them is 2% for the slant stack result and 2.7% for the picks-based result. The average difference between slant stack and picking results is 2.1%. We thus treat those results as practically equivalent. More
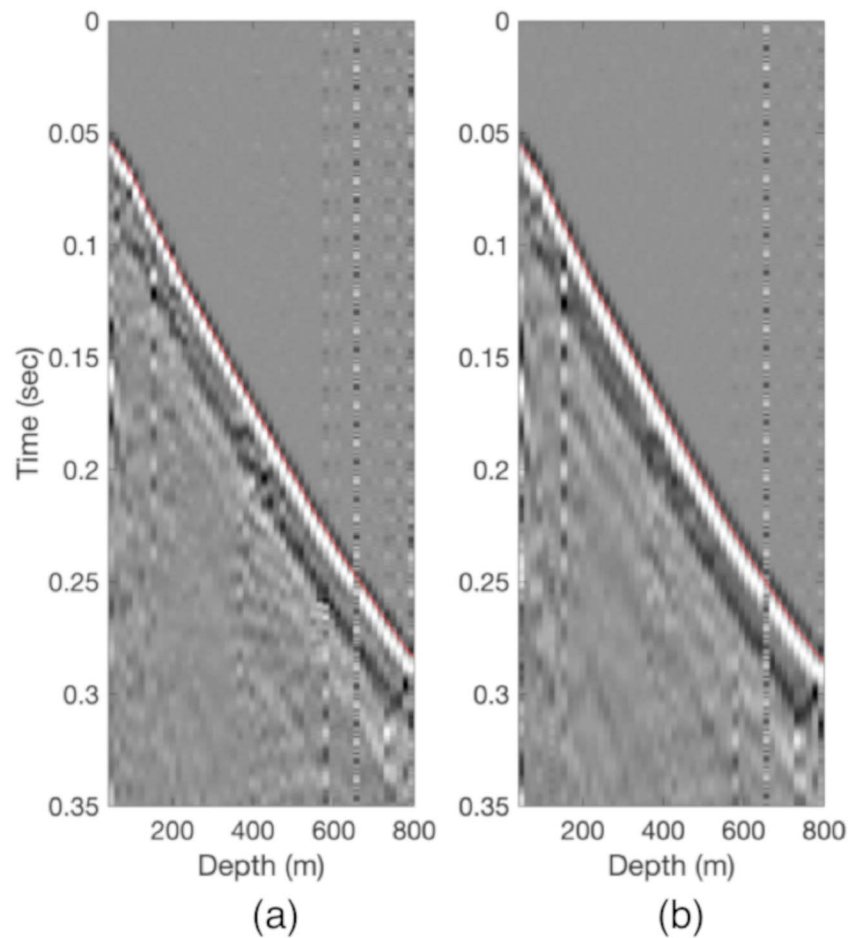
**Figure 8.** Vertical seismic profiling explosive sources recorded by downhole geophones. Two different explosive sources were used—5 lb (a) and 7 lb (b). Source and receiver locations are described in Figure 1. For both sources, picking the first break arrival is easy. It is overlaid in red, following the zero-crossing between negative (black) and positive (white) phases. The noisy channel at ~650 m is not picked, and we interpolate the arrival time using nearby channels.

importantly, they all seem to have the same overall structure—velocity increase up to about 300 m, fixed or slowly increasing velocity between 300 and 500 m, and velocity increase from 500 m and deeper. This structure follows the general trend set by the regional model but has a much higher resolution. Recovering high-resolution variations in the shallow subsurface, especially in nonreflective geology, is a major challenge for surface seismic. Therefore, it is not surprising that the regional model cannot obtain the same resolution. The model estimated from ambient field interferometry is of intermediate quality, between the regional and the high-resolution models. It is closer to the latter but appears to follow a somewhat linear trend, in contrast to the high-resolution models. This result is expected, as we compute the velocity model using low-frequency cross-correlation data. We emphasize that the interferometry analysis is relatively simple and uses 1-day-long data records.

The estimated $S$ model follows the high-resolution velocity structure of the $P$ model. The velocity model estimated using travel time picking is noisier. This is mostly due to interference with other seismic phases, as previously discussed. The $V_P/V_S$ shown in the right side seems to be significantly increasing when approaching the surface. Our analysis can be safely conducted at depths of 75 m and deeper, but from following the trend, it appears that at surface level values of $V_P/V_S = 3$ can be expected. The picking-based estimation of $V_P/V_S$ is noisy. There seems to be a significant high-value anomaly of $V_P/V_S$ around a depth of 500–520 m for both analysis methods, albeit it is more evident from the picking-based method. This is consistent with the change in velocity behavior we observe from 500 m and below. We believe we have an experimental observation confirming that $V_P/V_S$ anomaly.
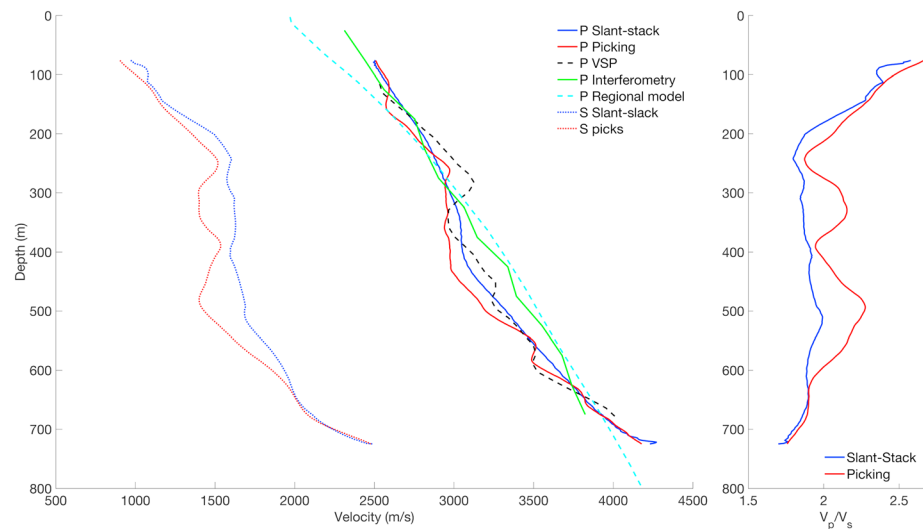
**Figure 9.** Estimated velocity models and $V_P/V_S$. We plot five $P$ velocity models: slant stack (blue) and travel time picking (red) results using the $M = 1.33$ earthquake record, conventional vertical seismic profiling (VSP) processing (black), ambient field interferometry (green), and regional model (cyan). We compute $S$ wave velocities using the same earthquake record and display slant stack (dotted blue) and picking-based (dotted red) results. The $V_P/V_S$ computed using slant stack (blue) and picking (red) results are shown on the right. Velocity models extracted from distributed acoustic sensing records and the VSP survey are close and follow the regional model trend. However, they seem to reveal more geological features. The interferometry is of intermediate quality. $V_P/V_S$ increases close to the surface using both methods. In addition, it shows a high-value anomaly at a depth of 500–520 m. This anomaly is evident from the picking-based model and noticeable in the slant stack estimation.

In Figure 10, we show the $M = 2.46$ earthquake, with true relative amplitude values (no trace normalization). This earthquake is an independent measurement, as the $V_P/V_S$ profile was computed without it. In a red rectangle, we highlight a specific event. It has a $P$ wave moveout, much like the coda $P$ events before and possibly after it. However, the event's amplitude is much stronger than the preceding coda $P$ waves. In addition, its phase behavior (negative-positive-negative) as well as its lower frequency distinguish it from coda $P$ waves. Therefore, we suggest that this event is a converted $SP$ mode, as $S$ arrivals are much stronger. It originates roughly at the 500-m-depth marker, indicative of a $P/S$ contrast.

Estimated velocity models are in agreement with previous geological knowledge of the area (Bradbury et al., 2007; Zoback et al., 2011). First, there is no sign of a strong of $P$ or $S$ wave velocity contrast in the estimated models. This is expected, as the granite contact is below the array. In addition, conventional surface surveys did not detect any reflective layer within the depth range of this study, as our velocity models suggest. Zimmer et al. (2007) showed that the $V_P/V_S$ of dry unconsolidated sands increases at low pressure. In fact, while three distinct areas emerge from separate $P$ and $S$ wave analysis, the $V_P/V_S$ indicates, in addition, a shallow, low-pressure area. The observed high $V_P/V_S$ values in the shallow section (<100 m) confirm the unconsolidated nature of the observed alluvial sediments. The structure we estimate thus consists of four major areas—unconsolidated sediments in the shallow section (below 100 m), sediments under compaction at 100–300 m, constant-velocity (fully compacted or low porosity) sediments at 300–500 m, and sediments under compaction at 500 to 800 m.

It is important to estimate the errors in retrieved velocity models in order to understand the validity and limitations of the suggested analysis. However, we use different methods to estimate the velocity models, and their input data's frequency content varies. Therefore, both the techniques used for error analysis and their input parameters will vary. For picking-based velocity estimation, we suggest adding a Gaussian picking error of zero mean and a certain standard deviation, depending on frequency content and signal-to-noise ratio, to the picked travel times. Then, the velocity profile is reestimated using the noisy picked travel times, including all spatial smoothing operators. This process is repeated 10,000 times to construct reasonable boundaries. For DAS earthquake records, we use standard deviations of 4 ms for $P$ wave picking and 20 ms for $S$ wave picking. We choose a standard deviation of 1 ms for the cross-correlated ambient field
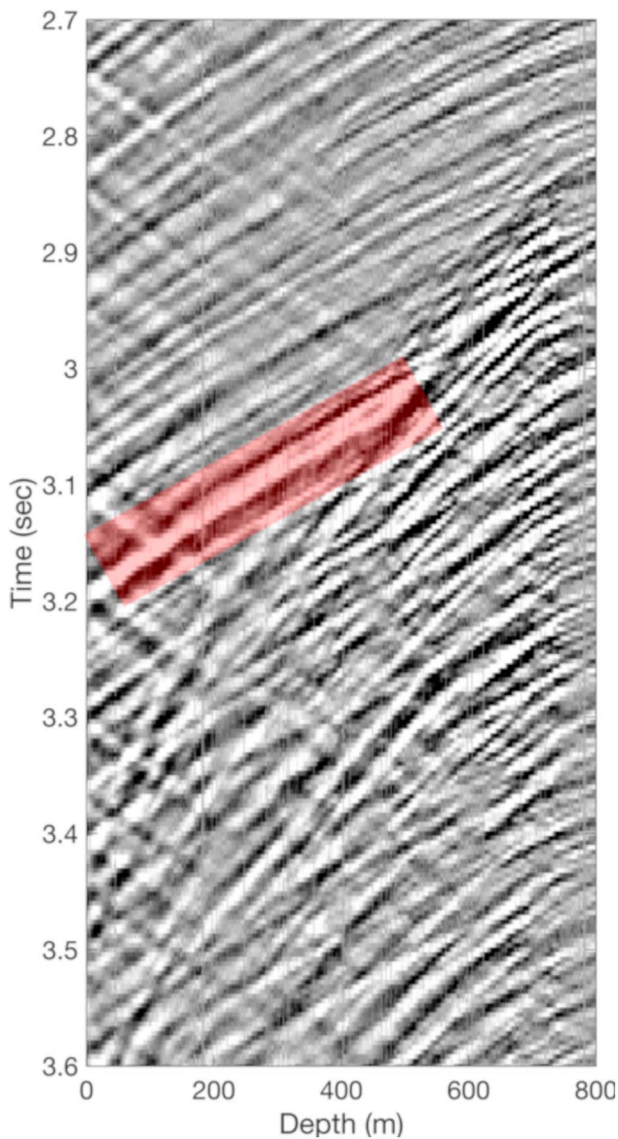
**Figure 10.** Highlighting of an *SP* converted event, shown at 0- to 120-Hz filtering. We display the record with constant gain, so relative amplitudes are preserved. The converted event is highlighted by a red rectangle. It has a clear *P* moveout and a high amplitude. Therefore, it seems to originate from the strong *S* phase. In addition, it is of lower frequency and has a different temporal behavior when compared to surrounding *P* coda waves.

waveforms and 1.25 ms for the conventional geophone survey. As previously described, the geophone survey is not 1-D by nature as sources are excited more than 40 m away from the wellhead. Therefore, we add an uncertainty component due to the potential error in accounting for the wavefronts' propagation path. We take the difference between the depth of the receivers, equivalent to a source at the wellhead, and the 2-D distance from the true source location to receivers as an upper bound of the possible traveled distance discrepancy. This uncertainty is added to the one arising from picking. For the slant stack approach, the error is estimated differently. We have previously explained how the maximal coherency value is chosen for each window. Such a value occurs at a given time sample and velocity. At that time sample, we test which velocities would yield a certain fraction of the maximal coherency. This velocity range defines the estimated error in the procedure. For the *P* wave estimation, we choose a threshold of 0.95 of the maximal coherency value. For the *S* waves, due to their interference with other seismic phases, we use a value of 0.8 instead.

In Figure 11, we show the results of the uncertainty analysis. Figure 11a contains the uncertainty of *P* wave velocity estimated from DAS earthquake records. It consists of the picking-based results (estimation in red and error in orange) and the slant stack ones (estimation in blue and error in dashed black). In Figure 11b, we show the estimated model (black) and uncertainty (gray) for the *P* wave velocity using the conventional geophone survey. In Figure 11c, the ambient field interferometry method is analyzed. The retrieved model (green) and uncertainty (cyan) for the *P* wave velocity are shown. In Figure 11d, we display *S* wave velocity estimation using DAS earthquake records. The picking results (model in red and uncertainty in orange) and slant stack (model in blue and uncertainty in dashed black) are shown. From this analysis, we draw several conclusions. First, models estimated by different data and techniques are within each other's uncertainty range. Nonetheless, even when taking into account the possible errors, our original interpretation, based on DAS earthquake records, appears to be stable. Second, the uncertainty increases with velocity. This is obvious in picking analysis from the fact that $V \propto 1/dt$ with $dt$ being the arrival time difference between two channels. For high velocities $V$, $dt$ is small. As a result, a constant uncertainty in travel time, like the one we model, will have a larger impact on the result than for a larger $dt$, representative of low velocities. The same effect plays a part in the slant stack analysis, but its explanation is less intuitive. Let us assume two close velocities, $V$ and $V + dV$. The slope difference between them, in time, is proportional to $\frac{1}{V} - \frac{1}{V+dV}$. By the definition of

the derivative, this is equal, in absolute value, to $dV/V^2$. In other words, the slope difference due to a $dV$ difference between two close velocities decreases proportionally to $V^2$. Therefore, the focusing power of the slant stack will decrease, and uncertainty will increase with velocity. Due to the same reasons, the error pattern is asymmetric. The positive (right) side is elongated compared to the negative (left) one. This explanation is compatible with the simple notion that higher velocities have longer wavelengths, and thus a lower resolution. Third, the ambient field model estimation suffers from a large uncertainty. This result is not surprising—the frequency content of the waveform after cross-correlation and stacking is lower than 20 Hz, whereas earthquake records contain usable information up to 80 Hz (for *S* waves) and 100 Hz (for *P* waves). Moreover, as stacking, necessary for increasing the signal-to-noise ratio of the cross-correlated waveforms, is based on the average velocity, it might be especially detrimental to the higher frequencies. In addition, the model is estimated at 50-m intervals. As a result, the errors do not smooth out as well as with earthquake records, in which the velocity is estimated every 1 m. Nonetheless, it is important to note that when
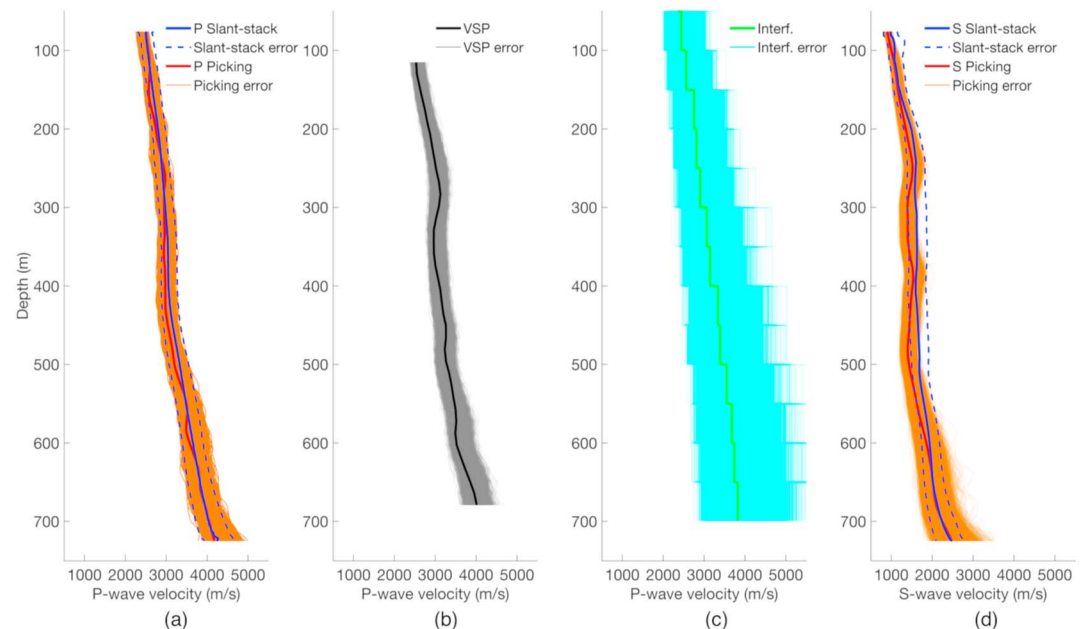
**Figure 11.** Error estimation for different velocity models. In (a), we show *P* wave velocity and error estimated using travel time picking and local slant stacks on distributed acoustic sensing earthquake records. We show the same analysis for the geophone survey (b) and interferometry (c). In (d), we show the velocity error and analysis for *S* wave velocity, applied on distributed acoustic sensing earthquake records, using travel time picking and local slant stacks. VSP vertical seismic profiling.

analyzing seven different cross-correlated waveforms, each arising from one day of data, the deviations between models are relatively small (less than 100 m/s standard deviation). Therefore, while the uncertainty may be high for this approach, the estimated models do not vary nearly as much in practice.

## 6. Discussion

In this study, we show how earthquakes recorded by downhole DAS systems can be used for *P* and *S* wave velocity estimation along the well. A recorded $M = 1.33$ earthquake at a distance of more than 10 km from the array has an average maximal usable frequency of ~70 Hz. It is higher than the conventional geophone survey, having ~55 Hz. In addition, geophones are positioned roughly every 15 m whereas the DAS array offers virtually continuous (1-m spacing) recording. In seismically active areas, recorded earthquakes of relatively low magnitudes can be a source of high-frequency data. In addition, such earthquakes propagate through the highly dissipative shallow section last, allowing for high-frequency content along most of their propagation path. Surface sources, on the contrary, immediately suffer from dissipation, thus reducing recorded frequency content.

For *P* waves, models estimated using two different analysis methods are within less than 3% absolute mean difference of a much more expensive VSP geophone survey. The methodology depends on earthquakes that propagate near vertically, but incidence angles of up to 15–20°, computed using straight rays, are judged acceptable. Moreover, earthquakes with higher incidence angles may also be used with appropriate scaling. Slant stack estimation of local velocity is automatic once several parameters have been chosen. These parameters are the size and shape of the spatial window, temporal window, and a minimum $V/V_S$. Travel time picking, on the contrary, requires manual choices, quality control, and possible manual intervention. While for our examples, it is relatively straightforward for *P* phases, this may not be the case for low signal-to-noise records. In addition, *S* wave processing is challenging even with high signal-to-noise data. It is due to *P* wave interference (coda waves, converted modes, and free surface reflections) as well as the directivity of the fiber, which lacks sensitivity to *S* phases propagating along it. Therefore, some preprocessing prior to picking is necessary. An alternative approach is to apply ambient field interferometry, which can be performed with as little as one day of continuous data. However, it does not recover *S* wave

velocities. Using a single day of recorded data, input correlograms for $P$ wave velocity estimation are of significantly lower-frequency content (5-20 Hz). Therefore, the retrieved $P$ wave model is of lower resolution.

Regardless of the velocity estimation method, the advantages of array-based processing are evident and stand out when handling $S$ phases. Records are very complex and consist of many different phases: direct $P$, $P$ coda, direct $S$, converted modes ($SP$, $PS$), $S$ coda, free surface reflections of all phases, and so forth. Trying to analyze $S$ arrivals using surface receivers only would be extremely challenging. Here, on the contrary, array-based filtering, based on event moveout with depth, can be applied and greatly simplify processing. It also allows for a better understanding of subsurface phenomena, like the $SP$-converted event we show. Thanks to its continuous sampling in depth, we can be much more certain of its interpretation, and even link it to computed velocity models.

Downhole DAS analysis is especially beneficial in recovering shallow velocity structures, which often remain unresolved by conventional seismic surveys. We unveil a more complex geological structure than previous studies describe. However, there is no disagreement between the two. Velocity estimation may also be a basis for different applications. For example, it can be conducted periodically to detect changes in velocity along the array. Ambient field interferometry is a natural candidate for such an application. Nonetheless, since monitoring is often conducted in seismically active areas, enough near-vertical earthquakes could be present for an event-based analysis. In addition, coda waves and converted modes may be looked into more systematically to refine velocity structures, especially in defining areas of contrast.

## 7. Conclusions

The array nature of the downhole DAS allows for advanced processing techniques, clear phase separation and understanding, and higher effective signal-to-noise ratio. Downhole DAS records can be used for velocity model estimation along the array. Relatively weak recorded earthquakes have a wide frequency content. Using records of near-vertically propagating earthquakes, $P$ and $S$ velocities are estimated using slant stacks and travel time picking. Obtained results match a $P$ wave model extracted from a conventional geophone-based VSP survey, which cannot yield an $S$ wave velocity model. The $P$ wave velocity profiles we obtain are much more detailed than a regional model estimated from surface seismic surveys. Interferometry is a useful alternative when no adequate earthquakes are recorded. A $P$ wave model computed using ambient field is superior to the regional model but not as detailed as the models extracted using recorded earthquakes. In addition, interferometry does not yield $S$ wave velocities. Application of earthquake-based analysis in the top 800 m of the SAFOD borehole reveals three distinct geological areas, concealed in the regional and interferometry-based models. $V_P/V_S$ analysis shows high values close to the surface, in accord with known alluvial sediments, and a high-ratio anomaly at a depth of 500 to 520 m. An SP converted mode event originating at this depth zone confirms a geological contrast.

## References

Ajo-Franklin, J., Dou, S., Daley, T. M., Freifeld, B., Robertson, M., Ulrich, C., et al. (2017). Timelapse surface wave monitoring of permafrost thaw using distributed acoustic sensing and a permanent automated seismic source. Paper presented at 87th SEG International Annual Meeting, Houston, TX. https://doi.org/10.1190/segam2017-17774027.1

Armstrong, T., McAteer, J., & Connolly, P. (2001). Removal of overburden velocity anomaly effects for depth conversion. *Geophysical Prospecting*, *49*(1), 79–99. https://doi.org/10.1046/j.1365-2478.2001.00238.x

Bakulin, A., & Calvert, R. (2006). The virtual source method: Theory and case study. *Geophysics*, *71*(4), SI139–SI150. https://doi.org/10.1190/1.2216190

Bakulin, A., Golikov, P., Smith, R., Erickson, K., Silvestrov, I., & Al-Ali, M. (2017). Smart DAS upholes for simultaneous land near-surface characterization and subsurface imaging. *The Leading Edge*, *36*(12), 1001–1008. https://doi.org/10.1190/tle36121001.1

Bensen, G. D., Ritzwoller, M. H., Barmin, M. P., Levshin, A. L., Lin, F., Moschetti, M. P., et al. (2007). Processing seismic ambient noise data to obtain reliable broad-band surface wave dispersion measurements. *Geophysical Journal International*, *169*(3), 1239–1260. https://doi.org/10.1111/j.1365-246X.2007.03374.x

Biondi, B. (1992). Velocity estimation by beam stack. *Geophysics*, *57*(8), 1034–1047. https://doi.org/10.1190/1.1443315

Biondi, B., Martin, E., Cole, S., Karrenbach, M., & Lindsey, N. (2017). Earthquakes analysis using data recorded by the Stanford DAS Array. Paper presented at 87th SEG International Annual Meeting, Houston, TX. https://doi.org/10.1190/segam2017-17745041.1

Bleibinhaus, F., Hole, J. A., Ryberg, T., & Fuis, G. S. (2007). Structure of the California Coast Ranges and San Andreas Fault at SAFOD from seismic waveform inversion and reflection imaging. *Journal of Geophysical Research*, *112*, B06315. https://doi.org/10.1029/2006JB004611

Blias, E. (2009). Stacking velocities in the presence of overburden velocity anomalies. *Geophysical Prospecting*, *57*(3), 323–341. https://doi.org/10.1111/j.1365-2478.2008.00750.x

Blum, J. A., Nooner, S. L., & Zumberge, M. A. (2008). Recording earth strain with optical fibers. *IEEE Sensors Journal*, *8*(7), 1152–1160. https://doi.org/10.1109/JSEN.2008.926882

Bradbury, K. K., Barton, D. C., Solum, J. G., Draper, S. D., & Evans, J. P. (2007). Mineralogic and textural analyses of drill cuttings from the San Andreas Fault Observatory at Depth (SAFOD) boreholes: Initial interpretations of fault zone composition and constraints on geologic models. *Geosphere*, *3*(5), 299–318. https://doi.org/10.1130/GES00076.1

Daley, T. M., Freifeld, B. M., Ajo-Franklin, J., Dou, S., Pevzner, R., Shulakova, V., et al. (2013). Field testing of fiber-optic distributed acoustic sensing (DAS) for subsurface seismic monitoring. *The Leading Edge*, *32*(6), 699–706. https://doi.org/10.1190/tle32060699.1

Daley, T. M., Miller, D. E., Dodds, K., Cook, P., & Freifeld, B. M. (2016). Field testing of modular borehole monitoring with simultaneous distributed acoustic sensing and geophone vertical seismic profiles at Citronelle, Alabama. *Geophysical Prospecting*, *64*(5), 1318–1334. https://doi.org/10.1111/1365-2478.12324

Dean, T., Cuny, T., & Hartog, A. H. (2017). The effect of gauge length on axially incident P-waves measured using fibre optic distributed vibration sensing. *Geophysical Prospecting*, *65*(1), 184–193. https://doi.org/10.1111/1365-2478.12419

Dou, S., Lindsey, N., Wagner, A. M., Daley, T. M., Freifeld, B., Robertson, M., et al. (2017). Distributed acoustic sensing for seismic monitoring of the near surface: A traffic-noise interferometry case study. *Scientific Reports*, *7*(1), 1–12. https://doi.org/10.1038/s41598-017-11986-4

Grattan, L. S., & Meggitt, B. T. (2000). *Optical Fiber Sensor Technology: Fundamentals*. Boston, MA: Springer. https://doi.org/10.1007/978-1-4757-6081-1

Hardage, B. A. (2000). *Vertical Seismic Profiling: Principles*. Oxford, UK: Pergamon.

Hole, J. A., Ryberg, T., Fuis, G. S., Bleibinhaus, F., & Sharma, A. K. (2006). Structure of the San Andreas fault zone at SAFOD from a seismic refraction survey. *Geophysical Research Letters*, *33*, L07312. https://doi.org/10.1029/2005GL025194

Hornman, J. C. (2017). Field trial of seismic recording using distributed acoustic sensing with broadside sensitive fibre-optic cables. *Geophysical Prospecting*, *65*(1), 35–46. https://doi.org/10.1111/1365-2478.12358

Jousset, P., Reinsch, T., Ryberg, T., Blanck, H., Clarke, A., Aghayev, R., et al. (2018). Dynamic strain determination using fibre-optic cables allows imaging of seismological and structural features. *Nature Communications*, *9*(1), 2509–2519. https://doi.org/10.1038/s41467-018-04860-y

Karrenbach, M., Kahn, D., Cole, S., Ridge, A., Boone, K., Rich J., et al. (2017). Hydraulic-fracturing-induced strain and microseismic using in situ distributed fiber-optic sensing. *The Leading Edge*, *36*(10), 837–844. https://doi.org/10.1190/tle36100837.1

Kostov, C., & Biondi, B. (1989). High-resolution velocity spectra using eigenstructure methods. *Geophysics*, *54*(7), 832–842. https://doi.org/10.1190/1.1442712

Landrø, M. (1999). Repeatability issues of 3-D VSP data. *Geophysics*, *19*(2), 75–84. https://doi.org/10.1037/a0016549

Lellouch, A., & Reshef, M. (2019). Velocity analysis and micro-seismic location improvement using moveout-corrected gathers. *Geophysics*, *84*(3), KS119–KS131. https://doi.org/10.1190/geo2018-0517.1

Lindsey, N. J., Martin, E. R., Dreger, D. S., Freifeld, B., Cole, S., James, S. R., et al. (2017). Fiber-optic network observations of earthquake wavefields. *Geophysical Research Letters*, *44*, 11,792–11,799. https://doi.org/10.1002/2017GL075722

Madsen, K. N., Tøndel, R., & Kvam, Ø. (2016). Data-driven depth calibration for distributed acoustic sensing. *The Leading Edge*, *35*(7), 610–614. https://doi.org/10.1190/tle35070610.1

Martin, E. R. (2018). Passive imaging and characterization of the subsurface with distributed acoustic sensing (Doctoral dissertation). Retrieved from SEP (http://sepwww.stanford.edu/data/media/public/docs/sep173/dissertation.pdf) Stanford, CA: Stanford University.

Martin, E. R., Biondi, B., Karrenbach, M., & Cole, S. (2017). Ambient noise interferometry from DAS array in underground telecommunications conduits. Paper presented in 79th EAGE Conference & Exhibition, Paris, France. https://doi.org/10.3997/2214-4609.201700743

Martin, E. R., & Biondi, B. L. (2018). Eighteen months of continuous near-surface monitoring with DAS data collected under Stanford University. Paper presented at 88th SEG International Annual Meeting, Anaheim, CA. https://doi.org/10.1190/segam2018-2997853.1

Martin, E. R., Castillo, C. M., Cole, S., Sawasdee, P. S., Yuan, S., Clapp, R., et al. (2017). Seismic monitoring leveraging existing telecom infrastructure at the SDASA: Active, passive, and ambient-noise analysis. *The Leading Edge*, *36*(12), 1025–1031. https://doi.org/10.1190/tle36121025.1

Martin, E. R., Lindsey, N. J., & Biondi, B. (2018). Introduction to Interferometry of Fiber Optic Strain Measurements. EarthArXiv, 14 June, 1–33. https://doi.org/10.31223/osf.io/s2tjd

Mateeva, A., Lopez, J., Mestayer, J., Wills, P., Cox, B., Kiyashchenko, D., et al. (2013). Distributed acoustic sensing for reservoir monitoring with VSP. *The Leading Edge*, *32*(10), 1278–1283. https://doi.org/10.1190/tle32101278.1

Mateeva, A., Lopez, J., Potters, H., Mestayer, J., Cox, B., Kiyashchenko, D., et al. (2014). Distributed acoustic sensing for reservoir monitoring with vertical seismic profiling. *Geophysical Prospecting*, *62*(4), 679–692. https://doi.org/10.1111/1365-2478.12116

Miyazawa, M., Snieder, R., & Venkataraman, A. (2008). Application of seismic interferometry to extract P- and S-wave propagation and observation of shear-wave splitting from noise data at Cold Lake, Alberta, Canada. *Geophysics*, *73*(4), D35–D40. https://doi.org/10.1190/1.2937172

Molyneux, J. B., & Schmitt, D. R. (1999). First-break timing: Arrival onset times by direct correlation. *Geophysics*, *64*(5), 1492–1501. https://doi.org/10.1190/1.1444653

Nakata, N., & Snieder, R. (2012). Estimating near-surface shear wave velocities in Japan by applying seismic interferometry to KiK-net data. *Journal of Geophysical Research*, *117*, B01308. https://doi.org/10.1029/2011JB008595

Neidell, N. S., & Taner, M. T. (1971). Semblance and other coherency measures for multichannel data. *Geophysics*, *36*(3), 482–497. https://doi.org/10.1190/1.1440186

Nosjean, N., Hanot, F., Gruffeille, J. P., & Miquelis, F. (2017). Statics: From imaging to interpretation pitfalls and an efficient way to overcome them. *First Break*, *368*(2), 148–157. https://doi.org/10.1016/0005-2728(74)90145-5

Papp, B., Donno, D., Martin, J. E., & Hartog, A. H. (2017). A study of the geophysical response of distributed fibre optic acoustic sensors through laboratory-scale experiments. *Geophysical Prospecting*, *65*(5), 1186–1204. https://doi.org/10.1111/1365-2478.12471

Parker, T., Shatalin, S., & Farhadiroushan, M. (2014). Distributed acoustic sensing—A new tool for seismic applications. *First Break*, *32*(2010), 61–69. https://doi.org/10.3997/1365-2397.2013034

Shapiro, N. M., & Campillo, M. (2004). Emergence of broadband Rayleigh waves from correlations of the ambient seismic noise. *Geophysical Research Letters*, *31*, L07614. https://doi.org/10.1029/2004GL019491

Spica, Z. J., Perton, M., Nakata, N., Liu, X., & Beroza, G. C. (2018). Site characterization at Groningen gas field area through joint surface-borehole H/V analysis. *Geophysical Journal International*, *212*(1), 412–421. https://doi.org/10.1093/gji/ggx426

Waldhauser, F., & Ellsworth, W. L. (2000). A Double-difference earthquake location algorithm: Method and application to the Northern Hayward Fault, California. *Bulletin of the Seismological Society of America*, *90*(6), 1353–1368. https://doi.org/10.1785/0120000006

Wang, H. F., Zeng, X., Miller, D. E., Fratta, D., Feigl, K. L., Thurber, C. H., & Mellors, R. J. (2018). Ground motion response to an $M_L$ 4.3 earthquake using co-located distributed acoustic sensing and seismometer arrays. *Geophysical Journal International*, *213*, 2020–2036. https://doi.org/10.1093/gji/ggy102

Wapenaar, K., & Fokkema, J. (2006). Green's function representations for seismic interferometry. *Geophysics*, *71*(4), SI33–SI46. https://doi.org/10.1190/1.2213955

Zeng, X., Lancelle, C., Thurber, C., Fratta, D., Wang, H., Lord, N., et al. (2017). Properties of noise cross-correlation functions obtained from a distributed acoustic sensing array at Garner Valley, California. *Bulletin of the Seismological Society of America*, *107*(2), 603–610. https://doi.org/10.1785/0120160168

Zhou, W., & Paulssen, H. (2017). P and S velocity structure in the Groningen gas reservoir from noise interferometry. *Geophysical Research Letters*, *44*, 11,785–11,791. https://doi.org/10.1002/2017GL075592

Zimmer, M. A., Prasad, M., Mavko, G., & Nur, A. (2007). Seismic velocities of unconsolidated sands: Part 1 — Pressure trends from 0.1 to 20 MPa. *Geophysics*, *72*(1), E1–E13. https://doi.org/10.1190/1.2399459

Zoback, M., Hickman, S., & Ellsworth, W. (2011). Scientific drilling into the San Andreas fault zone—An overview of SAFOD's first five years. *Scientific Drilling*, *22*(1), 14–28. https://doi.org/10.2204/iodp.sd.11.02.2011